Earth and Planetary Science Letters 507 (2019) 187–198

Contents lists available at ScienceDirect

Earth and Planetary Science Letters

www.elsevier.com/locate/epsl

Compositional and temperature effects on sulfur speciation and solubility in silicate melts

William M. Nash [a], Duane J. Smythe [a,*], Bernard J. Wood [a,b]

[a] Department of Earth Sciences, University of Oxford, South Parks Road, Oxford OX1 3AN, UK
[b] Department of Earth Sciences, University of Bristol, Bristol BS8 1RJ, UK

ARTICLE INFO

Article history:
Received 17 July 2018
Received in revised form 28 November 2018
Accepted 8 December 2018
Available online 19 December 2018
Editor: M. Bickle

Keywords:
sulfur
oxidation state
silicate melt
XANES
SIMS

ABSTRACT

We have determined the chemical speciation of dissolved sulfur and the sulfur concentration at fixed oxygen and sulfur fugacities for a wide range of silicate melt compositions (from Fe-rich basalt to dacite). Each melt was equilibrated at 1300 °C and 1-atmosphere pressure at oxygen fugacities (fO_2) between −1.67 and +1.6 log units relative to the Fayalite–Magnetite–Quartz (FMQ) buffer and absolute sulfur fugacities between −5.1 and −1.2 log units. The fO_2 and fS_2 of the experiments were controlled by using gas mixtures of CO–CO_2–SO_2. The speciation of sulfur in the quenched glasses was determined using both X-ray Absorption Near-Edge Spectroscopy (XANES), and from the dependence of equilibrium sulfur concentration on the fS_2/fO_2 ratio measured by secondary-ion mass spectrometry (SIMS) and electron microprobe.

The speciation of dissolved sulfur in each melt undergoes an abrupt transformation from S^{2-} to S^{6+} with increasing fO_2, and this transition is shifted ∼0.5 log units higher in fO_2 as melt FeO concentration increases from ∼5 wt% to ∼18 wt%. Since sulfide concentrations at constant fO_2 and fS_2 are consistently greater for more FeO-rich melts, the compositional effect on speciation may be explained by the well-known sensitivity of the sulfide capacity ($C_{S^{2-}}$) of the melt to FeO concentration.

S^{6+}/S^{2-} ratios for the glasses exhibit a linear relationship with Fe^{3+}/Fe^{2+}, indicating that the redox couples for iron and sulfur can be directly related to one another. We used thermodynamic data to model the interrelationship between Fe and S oxidation states in terms of the equilibrium

$$FeS + 8FeO_{1.5} = 8FeO + FeSO_4$$

Fitting the data to our experiments at 1300 °C we obtained the following expression for the temperature-dependence of speciation:

$$\log\left(\frac{S^{6+}}{S^{2-}}\right) = 8\log\left(\frac{Fe^{3+}}{Fe^{2+}}\right) + \frac{8.7436 \times 10^6}{T^2} - \frac{27703}{T} + 20.273$$

This equation fits the data for all our compositions and is also consistent with earlier results at 1050 °C and 950 °C. We used the interdependence of S and Fe oxidation states to infer electron transfer between Fe^{2+} and S^{6+} during quenching of glasses from Mauna Kea, Hawaii. The effect is sufficient to cause significant overestimation of equilibrium $Fe^{3+}/\Sigma Fe$ in natural glasses and corresponding overestimate of fO_2 by about 0.8 log units.

Glasses equilibrated under the most oxidizing conditions (containing S^{6+} only) have equilibrium S concentrations that are negatively correlated with their mole fractions of tetrahedral (Si + Ti) cations.

1. Introduction

Sulfur plays an important role in many geological environments. It is a major volatile component in volcanic systems in the form of SO_2 and H_2S gases; it is an essential nutrient in sulfate metabolism on the seafloor and it provides sulfide hosts for economically important elements such as Ni, Cu, Pt, and Au. This diverse range of

* Corresponding author.
E-mail address: duane.smythe@earth.ox.ac.uk (D.J. Smythe).

https://doi.org/10.1016/j.epsl.2018.12.006

properties is a result of the stabilities of several oxidation states of sulfur in natural environments. The relative stabilities of these different oxidation states control the distribution of sulfur between Earth's various geochemical reservoirs, core, mantle, crust, oceans and atmosphere. They also have profound influence on the distribution of many chalcophile (sulfur-loving) elements between these different reservoirs.

Although Earth's core has been estimated to contain about 1.7% S (Dreibus and Palme, 1995) the primitive mantle (bulk silicate Earth) contains only around 200 ppm S as FeS-rich sulfide (Palme and O'Neill, 2014). Despite this low abundance, however, the low solubility of sulfide in silicate melts (Li and Ripley, 2005; O'Neill and Mavrogenes, 2002; Smythe et al., 2017; Wendlant, 1982) means that mid-ocean ridge basalts (MORB), generated by partial melting of the mantle, are saturated in a liquid sulfide phase possibly throughout the entire liquid line of descent (Mathez, 1976). In this case, even very small amounts of sulfide control the concentrations of a number of nominally incompatible chalcophile elements such as Cu, Ag, Bi, Sb, Pb and the Pt-group metals in the equilibrium melts (Kiseeva and Wood, 2013, 2015). In contrast to MORB in which S is present almost entirely in the S^{2-} oxidation state, island arc rocks may exhibit saturation in either sulfide or sulfate (S^{6+}) the latter being stabilized at the higher oxygen fugacities (fO_2) recorded above some subduction zones (Carmichael, 1991; Jugo et al., 2010). In such cases the stabilizing of higher oxidation states leads to degassing of SO_2 an important agent of climate cooling.

The presence of sulfur is also significant in the evolution of other terrestrial bodies. The silicate surface of Mercury exhibits high S and low FeO contents and the planet is believed to be highly reduced (Nittler et al., 2011). Consistent with these interpretations are the high concentrations of S (up to 11 wt%) and low FeO contents (<1 wt%) observed experimentally in FeS-saturated silicate melts under strongly reducing conditions (Wohlers and Wood, 2017). Based on the compositions of SNC meteorites, Dreibus and Wänke (1985) noted strong depletions of chalcophile Co, Ni, Cu, In and Tl in silicate Mars relative to silicate Earth and suggested dissolution of greater fractions of these elements in Mars' core, together with a higher concentration of S (14.2%) in this reservoir. More recently, measurements of the compositions of Martian surface rocks by the Spirit Rover shows basalts containing up to 2.37% SO_3 (McSween et al., 2006). As sulfate is much more soluble than sulfide in silicate melts (Jugo et al., 2010) these observations suggest that S exhibits multiple oxidation states on Mars as well as Earth and that S^{6+} dominates in the near-surface environment.

Given the importance of both S^{2-} and S^{6+} in natural silicate melts on both Earth and Mars, our aim here has been to examine the conditions of fO_2 and fS_2 under which S^{2-} is replaced by S^{6+} as the stable oxidation state in silicate melts with high (Mars-like) and low (Earth-like) FeO contents.

1.1. Sulfur speciation in silicate melts

Fincham and Richardson (1954) showed that S^{2-} is the dominant S species in silicate melts at low fO_2 by demonstrating a linear relationship (with gradient 1/2) between log [S] (the sulfur content of the melt) and log (fS_2/fO_2). This relationship arises from dissolution of sulfide according to the following equilibrium:

$$\frac{1}{2}S_{2\ gas} + O^{2-}_{melt} = \frac{1}{2}O_{2\ gas} + S^{2-}_{melt} \tag{1}$$

The equilibrium constant (K_1) for this reaction is given by,

$$\log K_1 = \log \frac{fO_2^{1/2} \cdot aS^{2-}_{melt}}{fS_2^{1/2} \cdot aO^{2-}_{melt}} \tag{2}$$

By combining O^{2-} activity, the activity constant of S^{2-} and the equilibrium constant, we can then define the 'sulfide capacity' $C_{S^{2-}}$:

$$\log[S^{2-}] = \log C_{S^{2-}} + \frac{1}{2}\log\frac{fS_2}{fO_2} \tag{3}$$

The sulfide capacity is, for any given silicate melt, a function of its major element composition. From Equation (3) we see that for fixed melt composition, temperature and pressure log [S^{2-}] should depend on the log (fS_2/fO_2) with a one-half slope. Deviations from this slope indicate that S^{2-} is not the dominant sulfur species in the melt.

Under oxidizing conditions (i.e. fO_2's above the fayalite-magnetite-quartz, FMQ, oxygen buffer), Fincham and Richardson (1954) observed an increase in log [S] with increasing fO_2, indicating that sulfate becomes the dominant species under these conditions. This equilibrium can be expressed through the reaction:

$$\frac{1}{2}S_{2\ gas} + \frac{3}{2}O_{2\ gas} + O^{2-}_{melt} = SO^{2-}_{4\ melt} \tag{4}$$

As with sulfide, a sulfate capacity parameter ($C_{S^{6+}}$) can be defined and used to express the dependence of concentration on fO_2 and fS_2. From Equation (4) we define the equilibrium constant (K_4) as,

$$\log K_4 = \log \frac{aSO^{2-}_{4\ melt}}{fS_2^{1/2} \cdot fO_2^{3/2} \cdot aO^{2-}_{melt}} \tag{5}$$

We can then define the sulfate capacity ($C_{S^{6+}}$) by combining K_4, aO^{2-}_{melt}, and $\gamma SO^{2-}_{4\ melt}$. Rearranging yields:

$$\log[SO^{2-}_{4\ melt}] = \log C_{S^{6+}} + \frac{1}{2}\log fS_2 + \frac{3}{2}\log fO_2 \tag{6}$$

The transition from sulfide to sulfate with increasing fO_2 can readily be understood by combining reactions (1) and (4) as follows:

$$S^{2-}_{melt} + 2O_{2\ gas} = SO^{2-}_{4\ melt} \tag{7}$$

The stoichiometry of this equilibrium, specifically the large number of oxygen atoms required for oxidation, implies that the transition in stability between these species occurs over a narrow fO_2 range. This can be shown explicitly if the equilibrium is expressed in terms of the activities or concentrations of its components:

$$\log \frac{[SO^{2-}_4]_{melt}}{[S^{2-}]_{melt}} = \log K' + 2\log fO_2 \tag{8}$$

In Equation (8) activities have been approximated by concentrations and equilibrium constant K_7 replaced by K' (i.e. $K' = K_7 \cdot \gamma S^{2-}_{melt}/\gamma SO^{2-}_{4\ melt}$). The transition from S^{2-} to SO^{2-}_4, occurring over the expected narrow fO_2 interval, has been observed using the XANES method between FMQ and FMQ+2 by Jugo et al. (2010) and at FMQ by Klimm et al. (2012b). Compositional and temperature effects on the transition are unknown. The principal goal of our study was, therefore, to isolate these effects on speciation for a broad range of melt compositions.

1.2. Approaches to determining sulfur speciation

X-ray Absorption Near-Edge Structure (XANES) spectroscopy has been employed in several studies to measure the relative proportions of S^{6+} and S^{2-} in silicate glasses (Métrich et al., 2009; Botcharnikov et al., 2011; Brounce et al., 2017; Jugo et al., 2010). The large contrast in electron shielding between the S^{2-} and S^{6+} species gives rise to a difference of ~10 eV in K-edge energy

Table 1
Composition of starting materials in weight percent.

Composition	SiO_2	TiO_2	Al_2O_3	Cr_2O_3	FeO	MnO	MgO	CaO	Na_2O	K_2O	Total
JFR	45.1	1.5	13.1	0.1	17.4	0.4	8.9	9.6	3.8	0.0	100.0
DWF	51.4	0.4	8.1	0.4	19.8	0.6	12.7	6.3	0.4	0.0	100.0
PRI	50.0	1.3	12.5	0.0	10.5	0.2	16.1	9.4	0.0	0.0	100.0
EVO	53.7	3.8	10.6	0.0	18.6	0.4	4.7	8.2	0.0	0.0	100.0
AND	55.0	1.3	17.4	0.0	8.8	0.2	4.4	8.0	3.7	1.1	100.0
DAC	64.2	0.7	16.8	0.0	5.1	0.1	2.1	5.6	4.0	1.4	100.0

(Métrich et al., 2009) that is easily resolvable using XANES. Previous studies have demonstrated a positive correlation between the energy of the S *K*-edge and sulfur valence state (e.g. Paris et al., 2001; Fleet et al., 2005; Almkvist et al., 2010), making discrimination between intermediate species (e.g. S^{-}, S^{0}, S^{4+}) also possible. In our study, XANES was used to identify the sulfur species present in synthetic silicate glasses, and to determine their relative abundances by comparing the amplitudes of their characteristic absorption peaks.

An alternative way of estimating sulfur speciation is to determine the dependence of total sulfur concentration on fO_2 and fS_2. The observed relationships are then compared to the possible stoichiometries of the sulfur dissolution reactions such as (1) and (4) above. If the trends observed are consistent with a particular chemical equilibrium, the relevant sulfur species can be assumed to be dominant in the melt. This was the approach pursued by Fincham and Richardson (1954), and successfully extended to more geologically relevant melts by O'Neill and Mavrogenes (2002). Over the fO_2 range of the S^{2-} to S^{6+} transition the log fS_2 which can be obtained with commercial available gases at 1 atm is on the order of only −2.5 to −4.5, resulting in S concentrations in silicate melts as low as 1 ppm, well below the detection limit of electron probe micro-analysis (EPMA). We have therefore employed secondary-ion mass spectrometry (SIMS) for which the detection limit of S is ∼0.1 ppm. Both the spectroscopic and 'indirect' approaches to investigating speciation have been used in the present study.

2. Experimental methods

The silicate melt compositions investigated are given in Table 1 and were chosen to represent a broad range of terrestrial and Martian igneous rocks. The Martian basalts "JFR" and "DWF" are derived from the experimental products of Bertka and Holloway's (1994) study of Martian mantle melting (their Table 8), and represent ∼10% and ∼50% melts of a hypothetical model composition for Mars' mantle (Dreibus and Wanke, 1985). These experimentally derived compositions were used in preference to natural compositions, whose genetic relations to Mars' mantle are uncertain. The primitive and iron-rich model terrestrial basalts, "PRI" and "EVO", were generated by addition of olivine to an average MORB (from Gale et al., 2013) until equilibrium with Fo90.5 olivine was achieved at 1 bar pressure (to yield PRI), and subtraction of olivine and plagioclase to generate the iron-rich EVO composition. The andesitic and dacitic melts ("AND" and "DAC") are representative natural rock compositions from Carmichael et al. (1974).

The starting compositions were prepared from powdered oxides and carbonates, which were combined under ethanol into fine homogeneous powders, and decarbonated in air at 1000 °C. All experiments were conducted in a 1-atmosphere gas-mixing furnace at a constant temperature of 1300 °C, over an fO_2 range between FMQ-2 and FMQ+2 (extrapolated from the calibration of O'Neill (1987). Each experimental charge consisted of ∼10 mg of starting material which was suspended in the furnace on a loop of thin (0.25 mm) wire, stuck to the loop using paraffin oil. Rhenium wire was used below FMQ+1, while more oxidizing experiments (which would oxidize the Re metal) employed platinum as the loop material. Platinum loops were pre-saturated with Fe to minimize absorption from each charge. Experimental run conditions are given in Table 2.

The oxygen and sulfur fugacities were controlled by continuously flowing appropriate CO–CO_2–SO_2 gas mixtures through the furnace. The gas mixtures required at each fO_2 and fS_2 were calculated numerically from thermodynamic data for the various C–S and O-bearing species (Chase et al., 1985), following the procedure of White et al. (1958) and flow rates were controlled by standard mass-flow controllers. Based on numerous repeat measurements of fO_2 using an ytrria-stabilized zirconia electrolyte we estimate the uncertainty in fO_2 as ±0.1 log units. We chose the highest possible fS_2 at each fO_2 in order to maximize the sulfur concentration in the melt and obtain XANES spectra with high signal/noise ratios. To test whether sufficient time was allowed to reach equilibrium in our samples a set of experiments using the DAC composition were done under reducing conditions over a range of run durations. The concentration of sulfur was found to reach equilibrium between 8 and 12 h. All further experiments were run for a minimum of 12 h.

An important requirement of this study was the exposure of each melt composition to exactly the same conditions of temperature, pressure and fO_2, so that the influence of melt chemistry on sulfur redox state could be isolated. To this end the six charges were equilibrated simultaneously at each set of conditions, suspended together on a chandelier inside the furnace. The chandelier was drop-quenched in water at the end of each experiment. The recovered run-products were then mounted in epoxy and inspected under a petrographic microscope to ensure absence of crystalline phases and to test for presence of immiscible sulfides. Occasional very small Re–Fe sulfides, not quantitatively analyzable by microprobe, were found in some experiments performed on Re wires.

3. Analytical methods

3.1. Analysis of major-elements and sulfur

The major-element composition of each glass was determined by Wavelength Dispersive Spectroscopy using a Cameca SX5 electron microprobe at Oxford University. All analyses were conducted with a 15 kV accelerating voltage and a 10 µm, 30 nA electron beam. Standards used for silicate glass analysis were albite (Si, Na), synthetic periclase (Mg), pyrope (Al), sanidine (K), rutile (Ti), Mn metal, Cr metal, fayalite (Fe), and pyrite and barite (S). Peak count times of 20 s were used for Mg, Al, and Si, 30 s for Na, K, Ca, Ti, Cr, Mn, and Fe, and 90 s for S. A natural S-bearing basaltic glass (L17, Edinburgh ion probe facility) containing 48.5 wt% SiO_2, 13.2 wt% FeO*, and 1320 ppm S was used as a secondary standard. The limit of detection for S was ∼65 ppm. The JFR-1.67 glass (Table 2) was used to center the S peak for reduced compositions while the DWF+1.60 glass employed for oxidized compositions.

Sulfur concentrations in all experimental run products were determined by SIMS using a Cameca 1270 Mass Spectrometer at the Edinburgh University's Materials and Micro Analysis Centre (EMMAC). The JFR-1.67 glass (Table 2) was used as the primary stan-

Table 2
Run conditions, compositions and $S^{6+}/\Sigma S$ of experiments.

Sample	JFR+1.60	DWF+1.60	PRI+1.60	EVO+1.60	AND+1.60	DAC+1.60	JFR+1.21	DWF+1.21	PRI+1.21	EVO+1.21	AND+1.21	DAC+1.21	JFR+1.04	DWF+1.04	PRI+1.04	EVO+1.04
Duration (h)	12	12	12	12	12	12	12	12	12	12	12	12	12	12	12	12
$CO/CO_2/SO_2$ (1)	0/0/200	0/0/200	0/0/200	0/0/200	0/0/200	0/0/200	6/355/200	6/355/200	6/355/200	6/355/200	6/355/200	6/355/200	5/239/200	5/239/200	5/239/200	5/239/200
log fS_2	−5.00	−5.00	−5.00	−5.00	−5.00	−5.00	−5.03	−5.03	−5.03	−5.03	−5.03	−5.03	−4.51	−4.51	−4.51	−4.51
log fO_2	−5.70	−5.70	−5.70	−5.70	−5.70	−5.70	−6.13	−6.13	−6.13	−6.13	−6.13	−6.13	−6.29	−6.29	−6.29	−6.29
Fe^{3+}/Fe^{2+} (2)	0.30	0.24	0.28	0.24	0.32	0.33	0.26	0.21	0.26	0.23	0.28	0.28	0.24	0.21	0.25	0.21
n (EPMA)	10	10	10	10	10	10	10	10	10	10	10	10	10	10	10	10
SiO_2	45.84 (11)	49.89 (21)	48.12 (18)	51.92 (10)	53.97 (15)	65.60 (33)	46.78 (14)	53.02 (18)	51.37 (9)	55.11 (26)	55.58 (20)	64.95 (27)	48.66 (20)	55.33 (13)	52.20 (6)	55.57 (18)
TiO_2	1.46 (2)	0.41 (2)	1.23 (3)	3.71 (4)	1.32 (2)	0.67 (2)	1.56 (3)	0.45 (1)	1.39 (4)	3.96 (6)	1.36 (3)	0.68 (2)	1.63 (3)	0.49 (2)	1.40 (2)	4.10 (5)
Al_2O_3	12.46 (6)	7.73 (6)	11.71 (6)	10.02 (5)	16.55 (8)	16.30 (10)	13.11 (5)	8.41 (5)	12.75 (7)	10.98 (5)	17.09 (11)	16.46 (13)	13.62 (6)	8.97 (5)	13.07 (8)	11.09 (4)
Cr_2O_3	b.d.l.	0.04 (1)	b.d.l.	b.d.l.	b.d.l.	b.d.l.	0.09 (1)	0.17 (1)	b.d.l.	b.d.l.	b.d.l.	b.d.l.	0.10 (1)	0.17 (2)	b.d.l.	b.d.l.
FeO*	17.07 (7)	20.86 (13)	12.30 (9)	19.39 (7)	10.39 (7)	5.36 (8)	14.32 (5)	15.86 (7)	7.16 (4)	13.21 (14)	6.98 (13)	4.40 (20)	12.45 (9)	13.70 (5)	6.62 (6)	13.26 (8)
MnO	0.39 (2)	0.58 (2)	0.17 (2)	0.39 (2)	0.15 (1)	0.11 (1)	0.42 (2)	0.60 (2)	0.18 (1)	0.40 (2)	0.16 (2)	0.12 (1)	0.42 (2)	0.64 (1)	0.22 (2)	0.41 (2)
MgO	8.31 (5)	12.06 (10)	15.20 (8)	4.48 (4)	4.31 (6)	2.15 (2)	9.35 (6)	13.20 (6)	15.22 (9)	4.97 (5)	4.69 (5)	2.22 (3)	9.56 (9)	12.54 (10)	15.08 (15)	4.95 (4)
CaO	9.88 (5)	6.43 (4)	9.61 (6)	8.16 (4)	7.99 (5)	5.75 (8)	10.25 (5)	6.90 (4)	10.64 (6)	9.01 (5)	8.57 (6)	5.92 (5)	10.58 (3)	7.37 (6)	10.61 (5)	9.14 (5)
Na_2O	2.44 (3)	0.18 (1)	0.05 (1)	0.11 (1)	3.24 (3)	3.03 (4)	2.38 (4)	0.13 (1)	b.d.l.	b.d.l.	3.26 (5)	3.37 (6)	1.69 (2)	b.d.l.	b.d.l.	b.d.l.
K_2O	0.04 (1)	b.d.l.	b.d.l.	b.d.l.	0.68 (2)	1.00 (2)	b.d.l.	b.d.l.	b.d.l.	b.d.l.	0.79 (1)	1.12 (2)	b.d.l.	b.d.l.	b.d.l.	b.d.l.
S	b.d.l.	b.d.l.	128 (42)	b.d.l.	b.d.l.	b.d.l.	b.d.l.	b.d.l.	b.d.l.	b.d.l.	b.d.l.	b.d.l.	b.d.l.	b.d.l.	b.d.l.	b.d.l.
Total	97.81	97.99	98.24	97.86	98.11	99.67	98.26	98.75	98.71	97.64	98.46	99.23	98.71	99.22	99.19	98.52
$S^{6+}/\Sigma S$ (XANES)	0.900 (68)	0.901 (86)	0.941 (68)	0.930 (174)	0.954 (109)	–	–	–	–	–	–	–	–	–	–	–
n (SIMS)	3	3	3	3	3	3	3	3	3	3	4	4	3	3	3	3
S	84 (17)	41.0 (19)	89.3 (83)	16.1 (53)	19.3 (3)	3.73 (20)	3.82 (9)	2.29 (1)	1.22 (3)	1.71 (6)	1.63 (19)	1.49 (9)	6.47 (17)	4.28 (7)	2.69 (7)	3.91 (7)
$S^{6+}/\Sigma S$	0.990 (41)	0.979 (2)	0.997 (9)	0.950 (110)	0.992 (0)	0.993 (3)	0.682 (7)	0.480 (16)	0.705 (4)	0.343 (27)	0.863 (17)	0.975 (4)	0.584 (14)	0.384 (28)	0.704 (4)	0.365 (23)
$S^{6+}/\Sigma S_{(Corr.)}$ (3)	0.993 (41)	0.981 (2)	0.997 (9)	0.957 (110)	0.991 (0)	0.995 (3)	0.854 (2)	0.800 (2)	0.852 (2)	0.837 (2)	0.922 (15)	0.984 (4)	0.860 (2)	0.845 (1)	0.868 (1)	0.840 (1)

Sample	AND+1.04	DAC+1.04	JFR+0.62Pt	DWF+0.62Pt	PRI+0.62Pt	EVO+0.62Pt	AND+0.62Pt	DAC+0.62Pt	PRI+0.62	EVO+0.62	AND+0.62	DAC+0.62	JFR+0.13	PRI+0.13*	EVO+0.13	AND+0.13
Duration (h)	12	12	12	12	12	12	12	12	12	12	12	12	16	16	16	16
$CO/CO_2/SO_2$ (1)	5/239/200	5/239/200	6/167/200	6/167/200	6/167/200	6/167/200	6/167/200	6/167/200	6/167/200	6/167/200	6/167/200	6/167/200	12/136/200	12/136/200	12/136/200	12/136/200
log fS_2	−4.51	−4.51	−3.59	−3.59	−3.59	−3.59	−3.59	−3.59	−3.59	−3.59	−3.59	−3.59	−2.61	−2.61	−2.61	−2.61
log fO_2	−6.29	−6.29	−6.67	−6.67	−6.67	−6.67	−6.67	−6.67	−6.67	−6.67	−6.67	−6.67	−7.14	−7.14	−7.14	−7.14
Fe^{3+}/Fe^{2+} (2)	0.26	0.25	0.18	0.17	0.19	0.17	0.20	0.21	0.19	0.16	0.17	0.18	0.13	0.15	0.13	0.17
n (EPMA)	10	10	10	10	10	10	10	10	20	10	10	10	10	10	10	10
SiO_2	56.13 (12)	64.79 (35)	46.92 (15)	54.16 (15)	51.39 (11)	54.86 (9)	55.88 (17)	64.92 (140)	49.30 (14)	51.93 (8)	56.53 (20)	65.12 (26)	46.54 (9)	49.89 (11)	52.93 (10)	54.80 (47)
TiO_2	1.34 (2)	0.68 (3)	1.56 (4)	0.44 (2)	1.36 (3)	3.93 (3)	1.40 (3)	0.67 (3)	1.30 (2)	3.73 (3)	1.38 (3)	0.69 (2)	1.56 (3)	1.37 (3)	3.80 (3)	1.32 (3)
Al_2O_3	17.01 (6)	16.85 (10)	13.13 (2)	8.49 (4)	12.96 (6)	10.68 (8)	17.12 (11)	16.72 (34)	12.78 (7)	10.64 (5)	17.66 (9)	17.29 (5)	13.07 (6)	12.57 (7)	10.30 (6)	17.05 (12)
Cr_2O_3	b.d.l.	b.d.l.	0.11 (1)	0.19 (1)	b.d.l.	b.d.l.	b.d.l.	b.d.l.	b.d.l.	b.d.l.	b.d.l.	b.d.l.	0.13 (1)	b.d.l.	b.d.l.	b.d.l.
FeO*	7.30 (5)	4.88 (9)	15.97 (7)	15.23 (10)	7.83 (5)	15.00 (5)	7.84 (9)	5.32 (40)	10.80 (7)	18.78 (6)	9.13 (8)	5.86 (9)	18.31 (7)	10.59 (7)	18.57 (12)	9.03 (18)
MnO	0.15 (1)	0.14 (1)	0.43 (2)	0.61 (3)	0.19 (1)	0.41 (2)	0.16 (1)	0.12 (2)	0.18 (1)	0.39 (2)	0.16 (1)	0.13 (1)	0.39 (1)	0.19 (1)	0.39 (1)	0.14 (1)
MgO	4.49 (3)	2.38 (4)	9.19 (4)	13.06 (8)	14.83 (9)	4.77 (3)	4.72 (6)	2.27 (16)	14.41 (13)	4.57 (6)	4.61 (4)	2.43 (4)	9.25 (6)	14.34 (9)	4.59 (5)	4.51 (7)
CaO	8.44 (6)	6.28 (8)	10.19 (5)	7.03 (4)	10.48 (4)	8.79 (6)	8.70 (4)	6.01 (29)	10.22 (3)	8.52 (5)	8.60 (5)	6.15 (4)	10.05 (4)	10.24 (6)	8.31 (5)	8.45 (11)
Na_2O	3.14 (5)	2.73 (3)	1.02 (3)	b.d.l.	b.d.l.	b.d.l.	2.44 (3)	2.77 (6)	b.d.l.	b.d.l.	b.d.l.	1.12 (3)	b.d.l.	b.d.l.	b.d.l.	3.08 (5)
K_2O	0.78 (1)	0.71 (1)	b.d.l.	b.d.l.	b.d.l.	b.d.l.	0.27 (1)	0.68 (4)	b.d.l.	b.d.l.	b.d.l.	0.04 (1)	b.d.l.	b.d.l.	b.d.l.	0.70 (4)
S	b.d.l.	b.d.l.	b.d.l.	b.d.l.	b.d.l.	b.d.l.	b.d.l.	b.d.l.	b.d.l.	b.d.l.	b.d.l.	b.d.l.	101 (30)	b.d.l.	b.d.l.	b.d.l.
Total	98.78	99.44	98.51	99.21	99.04	98.44	98.55	99.47	99.01	98.57	98.07	98.82	98.72	98.82	98.30	98.93
$S^{6+}/\Sigma S$ (XANES)	–	–	0.392 (27)	0.409 (33)	–	–	–	–	–	–	–	–	0.073 (7)	0.151 (19)	0.063 (8)	0.131 (14)
n (SIMS)	5	3	3	3	3	3	3	3	3	3	3	3	3	3	3	4
S	3.6 (12)	2.32 (82)	33.5 (3)	20.0 (4)	8.29 (11)	21.4 (3)	7.89 (60)	2.49 (29)	15.2 (2)	43.7 (19)	8.32 (34)	3.05 (38)	100 (1)	31.0 (3)	90.5 (17)	31.2 (29)
$S^{6+}/\Sigma S$	0.863 (111)	0.964 (126)	0.588 (13)	0.324 (41)	0.506 (13)	0.405 (18)	0.678 (29)	0.828 (14)	0.730 (3)	0.708 (5)	0.694 (22)	0.860 (16)	–	0.265 (55)	0.189 (71)	0.532 (73)
$S^{6+}/\Sigma S_{(Corr.)}$ (3)	0.919 (108)	0.973 (126)	0.737 (4)	0.755 (3)	0.719 (3)	0.764 (2)	0.768 (17)	0.855 (14)	0.736 (3)	0.744 (4)	0.725 (18)	0.866 (16)	–	0.291 (47)	0.265 (42)	0.567 (60)

Table 2 (*continued*)

Sample	DAC+0.13	JFR-0.19	DWF-0.19	PRI-0.19	EVO-0.19	AND-0.19	JFR-0.41	DWF-0.41	EVO-0.41	AND-0.41	DAC-0.41	JFR-0.70	DWF-0.70	PRI-0.70	EVO-0.70	AND-0.70
Duration (h)	16	13	13	13	13	13	16.5	16.5	16.5	16.5	16.5	28	28	28	28	28
$CO/CO_2/SO_2$ (1)	12/136/200	21/85/153	21/85/153	21/85/153	21/85/153	21/85/153	19/95/62	19/95/62	19/95/62	19/95/62	19/95/62	46/188/62	46/188/62	46/188/62	46/188/62	46/188/62
$\log fS_2$	−2.61	−1.95	−1.95	−1.95	−1.95	−1.95	−1.96	−1.96	−1.96	−1.96	−1.96	−1.88	−1.88	−1.88	−1.88	−1.88
$\log fO_2$	−7.14	−7.47	−7.47	−7.47	−7.47	−7.47	−7.70	−7.70	−7.70	−7.70	−7.70	−8.00	−8.00	−8.00	−8.00	−8.00
Fe^{3+}/Fe^{2+} (2)	0.13	0.11	0.10	0.13	0.11	0.12	0.10	0.10	0.10	0.11	0.11	0.10	0.08	0.10	0.09	0.09
n (EPMA)	10	10	10	10	10	10	10	10	10	10	10	10	10	10	10	10
SiO_2	65.75 (11)	46.14 (11)	50.61 (15)	49.90 (11)	51.98 (14)	56.57 (27)	45.85 (22)	51.61 (11)	52.96 (10)	56.58 (13)	64.79 (16)	45.29 (6)	51.04 (9)	49.42 (15)	52.13 (13)	56.08 (15)
TiO_2	0.70 (2)	1.53 (3)	0.42 (1)	1.31 (2)	3.82 (3)	1.39 (2)	1.55 (2)	0.44 (1)	3.79 (4)	1.46 (2)	0.73 (2)	1.50 (3)	0.43 (1)	1.32 (3)	3.77 (4)	1.39 (2)
Al_2O_3	17.41 (10)	13.32 (5)	8.37 (6)	12.91 (6)	10.45 (4)	17.77 (5)	12.87 (6)	7.86 (3)	10.25 (4)	17.61 (8)	17.98 (5)	13.12 (5)	8.21 (4)	12.83 (5)	10.40 (4)	17.94 (8)
Cr_2O_3	b.d.l.	0.14 (1)	0.20 (2)	b.d.l.	b.d.l.	b.d.l.	0.14 (1)	0.23 (1)	b.d.l.	b.d.l.	b.d.l.	0.13 (1)	0.25 (1)	b.d.l.	b.d.l.	b.d.l.
FeO*	6.01 (10)	18.35 (5)	20.27 (10)	10.50 (6)	19.10 (6)	9.38 (8)	18.34 (10)	19.53 (12)	18.45 (7)	9.53 (6)	5.99 (4)	18.04 (7)	19.87 (8)	10.88 (4)	18.82 (7)	9.40 (7)
MnO	0.13 (1)	0.41 (2)	0.58 (2)	0.19 (2)	0.38 (2)	0.16 (1)	0.41 (2)	0.58 (2)	0.41 (2)	0.16 (1)	0.13 (1)	0.41 (1)	0.58 (2)	0.18 (1)	0.40 (1)	0.15 (1)
MgO	2.46 (3)	9.12 (6)	12.37 (6)	14.53 (5)	4.57 (5)	4.60 (3)	8.80 (13)	12.51 (7)	4.60 (4)	4.60 (4)	2.43 (4)	9.04 (11)	12.71 (8)	14.35 (12)	4.63 (3)	4.66 (4)
CaO	6.15 (5)	10.11 (5)	6.58 (4)	10.23 (5)	8.49 (6)	8.61 (4)	10.03 (5)	6.57 (3)	8.46 (4)	8.54 (7)	6.31 (4)	9.95 (4)	6.64 (5)	10.37 (5)	8.52 (4)	8.54 (6)
Na_2O	0.18 (1)	b.d.l.	b.d.l.	b.d.l.	b.d.l.	b.d.l.	b.d.l.	b.d.l.	b.d.l.	b.d.l.	0.48 (1)	1.64 (3)	b.d.l.	b.d.l.	b.d.l.	0.04 (1)
K_2O	b.d.l.	b.d.l.	b.d.l.	b.d.l.	b.d.l.	b.d.l.	b.d.l.	b.d.l.	b.d.l.	b.d.l.	b.d.l.	b.d.l.	b.d.l.	b.d.l.	b.d.l.	b.d.l.
S	b.d.l.	258 (20)	292 (16)	97 (14)	243 (19)	b.d.l.	290 (20)	308 (22)	260 (31)	94 (24)	b.d.l.	714 (23)	608 (22)	198 (12)	526 (25)	202 (19)
Total	98.19	99.16	99.43	99.58	98.81	98.49	97.48	98.49	97.94	97.65	97.97	99.20	99.78	99.37	98.72	98.22
$S^{6+}/\Sigma S$ (XANES)	–	0.041 (3)	0.049 (3)	0.009 (7)	0.027 (3)	0.228 (19)	0.012 (3)	0.046 (4)	0.007 (3)	0.045 (10)	–	0.007 (1)	0.003 (3)	0.029 (3)	0.006 (3)	0.000 (41)
n (SIMS)	3	3	3	3	3	4	3	3	3	3	3	3	3	3	3	3
S	1.88 (36)	234 (2)	246 (3)	69.3 (12)	226 (3)	27.9 (25)	266 (1)	257 (1)	243 (1)	70.2 (4)	10.9 (5)	663 (9)	540 (7)	172 (2)	510 (3)	151 (8)
$S^{6+}/\Sigma S$	0.000 (0)	0.000 (0)	0.000 (0)	0.000 (0)	0.000 (0)	0.000 (0)	0.000 (0)	0.000 (0)	0.000 (0)	–	–	0.311 (67)	–	–	–	–
$S^{6+}/\Sigma S_{(Corr.)}$ (3)	0.000 (0)	0.000 (0)	0.000 (0)	0.000 (0)	0.000 (0)	0.000 (0)	0.000 (0)	0.000 (0)	0.000 (0)	–	–	0.360 (50)	–	–	–	–

Sample	JFR-0.94	DWF-0.94	PRI-0.94	EVO-0.94	AND-0.94	DAC-0.94	JFR-1.67	DWF-1.67	PRI-1.67	EVO-1.67	AND-1.67	DAC-1.67	DTS-02	DTS-08	DTS-12	DTS-24
Duration (h)	12	12	12	12	12	12	24	24	24	24	24	24	2	8	12	24
$CO/CO_2/SO_2$ (1)	48/165/33	48/165/33	48/165/33	48/165/33	48/165/33	48/165/33	148/99/48	148/99/48	148/99/48	148/99/48	148/99/48	148/99/48	148/99/48	148/99/48	148/99/48	148/99/48
$\log fS_2$	−1.87	−1.87	−1.87	−1.87	−1.87	−1.87	−1.21	−1.21	−1.21	−1.21	−1.21	−1.21	−1.21	−1.21	−1.21	−1.21
$\log fO_2$	−8.24	−8.24	−8.24	−8.24	−8.24	−8.24	−8.98	−8.98	−8.98	−8.98	−8.98	−8.98	−8.98	−8.98	−8.98	−8.98
Fe^{3+}/Fe^{2+} (2)	0.08	0.08	0.09	0.08	0.09	0.09	0.06	0.06	0.07	0.06	0.07	0.07	0.08	0.07	0.07	0.07
n (EPMA)	10	10	10	10	10	10	30	10	10	10	10	10	10	10	10	10
SiO_2	46.36 (14)	50.77 (27)	49.48 (18)	51.76 (20)	56.3 (18)	64.92 (41)	45.74 (32)	50.08 (29)	49.92 (45)	52.43 (11)	55.68 (7)	64.86 (23)	63.95 (47)	65.07 (81)	64.52 (83)	64.70 (17)
TiO_2	1.56 (2)	0.44 (2)	1.32 (2)	3.76 (3)	1.33 (3)	0.71 (3)	1.55 (3)	0.44 (3)	1.37 (3)	3.76 (4)	1.37 (2)	0.72 (1)	0.76 (10)	0.69 (2)	0.71 (3)	0.68 (1)
Al_2O_3	13.31 (7)	8.15 (9)	13.07 (5)	10.43 (4)	17.61 (8)	17.66 (12)	13.06 (44)	7.50 (5)	12.72 (11)	10.21 (5)	17.00 (7)	16.92 (20)	16.76 (14)	16.38 (40)	16.67 (32)	16.87 (8)
Cr_2O_3	0.13 (0)	0.26 (1)	b.d.l.	b.d.l.	b.d.l.	b.d.l.	0.13 (1)	0.35 (1)	b.d.l.	b.d.l.	b.d.l.	b.d.l.	b.d.l.	b.d.l.	b.d.l.	b.d.l.
FeO*	18.17 (4)	20.03 (5)	10.69 (6)	18.87 (9)	9.19 (8)	5.69 (16)	17.96 (33)	20.14 (10)	10.44 (6)	18.48 (6)	8.83 (6)	5.38 (11)	4.91 (25)	5.13 (20)	5.22 (32)	5.24 (7)
MnO	0.41 (1)	0.60 (1)	0.18 (1)	0.41 (2)	0.15 (2)	0.13 (1)	0.41 (2)	0.58 (2)	0.19 (1)	0.39 (1)	0.13 (1)	0.12 (1)	0.11 (2)	0.12 (2)	0.12 (1)	0.13 (1)
MgO	9.39 (9)	12.71 (18)	14.60 (12)	4.58 (5)	4.64 (11)	2.38 (6)	9.10 (16)	12.74 (5)	13.85 (14)	4.62 (6)	4.45 (5)	2.27 (4)	2.22 (6)	2.17 (7)	2.28 (13)	2.35 (5)
CaO	10.25 (6)	6.61 (6)	10.28 (6)	8.50 (5)	8.57 (5)	6.16 (7)	9.97 (6)	6.63 (5)	10.22 (14)	8.30 (4)	8.23 (3)	6.00 (11)	5.80 (13)	5.82 (14)	5.96 (27)	6.19 (4)
Na_2O	0.06 (1)	0.04 (1)	b.d.l.	0.06 (1)	1.27 (3)	2.07 (4)	0.36 (1)	0.46 (2)	0.34 (2)	0.56 (1)	1.69 (2)	2.49 (3)	3.64 (4)	2.99 (4)	2.86 (3)	2.34 (5)
K_2O	b.d.l.	b.d.l.	b.d.l.	b.d.l.	0.03 (1)	0.15 (1)	b.d.l.	0.04 (1)	0.04 (1)	0.09 (1)	0.26 (1)	0.49 (1)	1.38 (4)	0.96 (4)	0.83 (3)	0.44 (1)
S	723 (24)	774 (29)	243 (22)	710 (32)	141 (19)	b.d.l.	2121 (38)	2397 (33)	648 (23)	2001 (38)	410 (64)	78 (13)	b.d.l.	164 (39)	186 (23)	196 (28)
Total	99.71	99.68	99.64	98.45	99.10	99.88	98.49	99.20	98.33	99.05	97.69	99.26	99.52	99.39	99.19	98.95
$S^{6+}/\Sigma S$ (XANES)	0.006 (3)	0.004 (2)	0.000 (22)	0.000 (11)	0.016 (9)	–	0.002 (1)	0.002 (2)	0.005 (1)	0.0003 (8)	0.09 (1)	–	–	–	–	–
n (SIMS)	3	3	3	3	3	3	5	3	3	3	3	3	4	4	3	3
S	709 (3)	772 (4)	221 (2)	694 (6)	98 (4)	15.7 (12)	2121 (14)	2326 (18)	621 (2)	2031 (1)	370 (8)	91 (12)	43 (42)	106 (51)	142 (2)	144 (8)
$S^{6+}/\Sigma S$	–	–	–	–	0.000 (0)	0.000 (0)	0.000 (0)	0.000 (0)	0.000 (0)	0.000 (0)	0.000 (0)	0.000 (0)	–	–	–	–
$S^{6+}/\Sigma S_{(Corr.)}$ (3)	–	–	–	–	0.000 (0)	0.000 (0)	0.000 (0)	0.000 (0)	0.000 (0)	0.000 (0)	0.000 (0)	0.000 (0)	–	–	–	–

Notes: *n* = number of analysis; b.d.l. = below detection limit; *XANES spectra indicate the presence of Re–Fe sulfide; (1) Gas flow rates in standard cubic centimeters per min; (2) Calculated using the method of Kress and Carmicheal (1991); (3) S^{2-} corrected for Fe and alkali loss using the model of Smythe et al. (2017). Experiments equilibrated at $\log fO_2$ of −6.68 (labeled Pt) and above were suspended in the furnace using Pt wire all others used Re wire. All experiments were done at 1300 °C and 1 bar. Errors in parentheses given to the last significant figures.

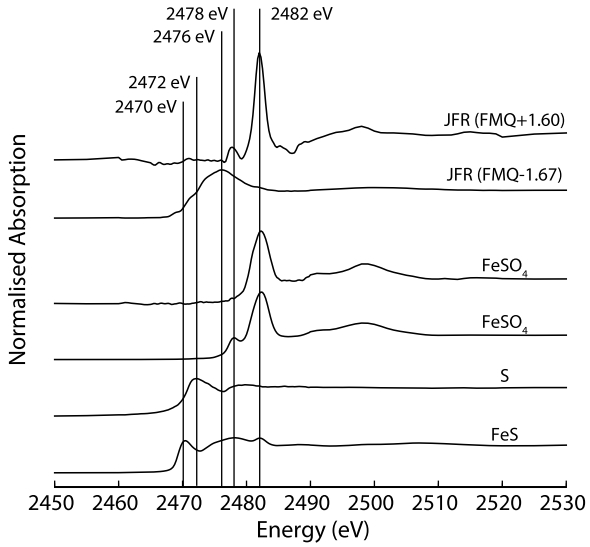

Fig. 1. Normalized S *K*-edge XANES spectra of standard materials (lowermost four spectra) and the 'JFR' melt under fully oxidized (FMQ+1.6) and fully reduced (FMQ-1.67) conditions. The spectral features characteristic of the sulfur species present in each case are indicated, and their energies labeled. The two $FeSO_4$ spectra demonstrate the influence of beam intensity. The upper spectrum, collected at an X-ray fluence lower than 4×10^8 photon/μm^2 s, lacks the 2478 eV peak indicative of photoreduction by the beam. The broad feature at 2476 eV in the reduced JFR melt – present as a shoulder in the FeS standard spectrum – is assumed to indicate sulfide, following analysis of similar glassy silicates by Jugo et al. (2010) and Klimm et al. (2012a). Minor oxidation in the FeS standard is indicated by the small feature at 2482 eV.

dard for all sulfur measurements and the L17 glass was employed as a secondary standard. A cesium primary ion beam was used, and the instrument calibrated using ^{18}O since preliminary analyses revealed ^{18}O and ^{32}S to have similar ion yields.

3.2. XANES

Sulfur *K*-edge XANES spectra were collected on the I18 beamline at the Diamond Light Source synchrotron facility (UK). Spectra were obtained using the Si(111) monochromator, with the instrument in fluorescence mode. The take-off angle was 40°. An energy step-size of 0.25 eV was used across the XANES region, which was broadened to 5 eV at the spectrum extremities to minimize acquisition time while collecting sufficient data for good spectrum normalization. Multiple spectra were collected for selected glasses to verify instrumental reproducibility.

To minimize potential modification of S^{6+}/S^{2-} during XANES analysis as noted by Wilke et al. (2008) and Jugo et al. (2010), a defocused beam (50 × 50 μm square) was used with the lowest fluence available ($\sim 10^{12}$ photon/s). The sample, detector, and beam-source were enclosed by a He-filled bag to minimize X-ray absorption and maintain acceptable signal/noise ratios at these low fluences. This configuration was found to eliminate most modification of the sulfur redox state under exposure to the X-ray beam as can be seen by the two $FeSO_4$ spectra in Fig. 1. The upper spectrum, collected under low-fluence conditions, lacks the small peak at 2478 eV that is present in the high-fluence spectrum below. The latter is indicative of photo-reduction by the beam.

4. Results

4.1. Interpretation of XANES spectra

Following the methodology of previous researchers (e.g. Jugo et al., 2010) we adopted an empirical approach to determining speciation by correlating spectral features with specific ionic species in the glasses. These associations are established using spectra of our standards as well as the findings of previous workers. Three standards (FeS, S, and $FeSO_4$ powders) were analyzed to define the edge positions of the different sulfur species, and to explore the potential for beam-induced damage. Fig. 1 presents the spectra of these standards, as well as samples JFR-1.67 and JFR+1.60.

The FeS spectrum exhibits a sharp peak at 2470.4 eV, and a much broader one at 2478 eV. The 2470.4 eV peak corresponds to 1*s* to 3*p* and 3*d* transitions (Wilke et al., 2011) and its amplitude has been shown to depend on the cation that S^{2-} is bonded to; transition metal sulfides exhibit a large peak at the energy, and sulfides of Ca and Mg exhibit none at all (Fleet et al., 2005). The broader feature represents a combination of 1*s* and 3*p* transitions and multiple scattering resonances and is invariably associated with the sulfide ion (Wilke et al., 2011). Sulfide-saturated basaltic glasses (both natural and synthetic) examined by Jugo et al. (2010) and Fleet et al. (2005) exhibit a similar broad feature at this energy, with subtle variations in edge shape that presumably depend on the local bonding environment. Each of the six glasses in this study display this feature when equilibrated under the most reducing conditions, consistent with the dominance of sulfide at low fO_2.

The $FeSO_4$ standard exhibits a single sharp peak at 2482 eV, which is characteristic of excitations from the sulfur 1*s* to the sulfur 3*p* and oxygen 2*p* orbitals of the SO_4^{2-} anion (Wilke et al., 2011). XANES spectra for sulfate compounds analyzed by previous workers have consistently shown this feature (e.g. Jugo et al., 2010; Klimm et al., 2012a; Almkvist et al., 2010), and it dominates the spectra of all six melt compositions prepared at the highest fO_2, indicating that S^{6+} is the stable sulfur species under the most oxidizing conditions. A small peak at this energy is also evident in the spectrum for the FeS standard, suggesting that our FeS powder has undergone some minor oxidation.

Both the high-fluence $FeSO_4$ standard and each of the most oxidized silicate melts (e.g. JFR+1.60 shown in Fig. 1) exhibit a small peak at 2478 eV, characteristic of the sulfite (S^{4+}) ion (Métrich et al., 2002). The absence of this peak in the $FeSO_4$ spectrum collected at low-fluence indicates that it is a product of beam damage rather than a feature intrinsic to the standard as shown by Wilke et al. (2008) and Jugo et al. (2010).

4.2. Speciation trends in the experimental glasses

For each of the six melt compositions studied, the sequence of spectra representing equilibrium under progressively more oxidizing conditions display a diminution of the broad feature at 2476 eV, and its replacement by the sharper peak at 2482 eV. Each melt composition therefore undergoes the expected transition between sulfide and sulfate stability with increasing fO_2. The sequences of spectra for all 6 melts are shown in Fig. 2. Note that the XANES spectra for JFR, PRI, EVO and DWF melts are particularly sensitive to presence of small amounts of sulfate at low fO_2 and that this makes the XANES method complementary to SIMS analysis. The latter is more accurate at high S^{6+}/S^{2-} as discussed below. An increase in spectrum noise with increasing oxidation state is evident, consistent with an observed decrease in S concentration with increasing fO_2 (Table 2). From Fig. 2 we can also observe, at fixed fO_2 increasing S^{2-}/S^{6+} with increasing FeO content of the silicate melt. This is consistent with the observed increase of sulfide capacity ($C_{S^{2-}}$) with increasing FeO content (O'Neill and Mavrogenes, 2002). One spectrum (PRI at FMQ+0.13, Fig. 2) was measured on an area of glass containing a Re–Fe sulfide inclusion.

Backgrounds for each spectrum were subtracted using a cubic spline function and spectra were normalized to a post edge intensity of 1. The fractions of S^{2-} and S^{6+} in our glasses (Table 2) were then calculating from the area ratios of the S^{2-} and S^{6+} peaks us-

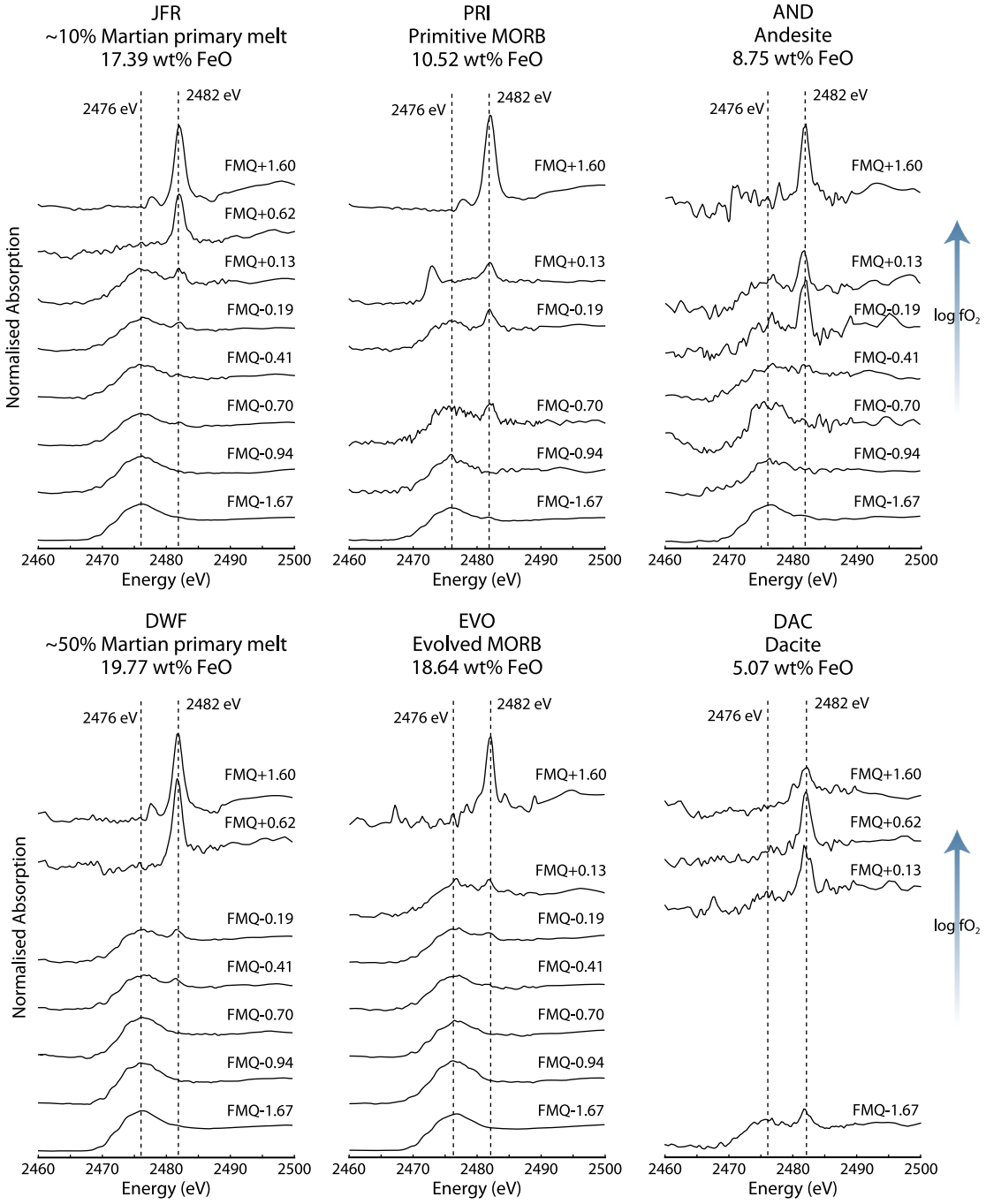

Fig. 2. The complete series of S K-edge XANES spectra for the synthetic glasses investigated in this study. Spectra positioned higher in each series represent experiments performed under more oxidizing conditions (fO_2 conditions labeled relative to FMQ). The change in speciation between sulfide and sulfate is indicated by the progressive diminution of the peak at 2476 eV and the growth of the peak of 2482 eV. Signal/noise ratios generally decrease with increasing fO_2 due to decreasing S concentration. Horizontally adjacent spectra represent melts at identical fO_2 conditions, and comparisons between these – where permitted by an adequate signal/noise ratio – suggests that melts with higher FeO content stabilize sulfate at higher fO_2. Note that primitive MORB at FMQ+0.13 contains Re–Fe sulfide inclusions.

ing the peak fitting software Fityk (Wojdyr, 2010). To correct for the greater X-ray absorbance of sulfate relative to sulfide (Jugo et al., 2010; Jalilehvand, 2006) we applied the "generic scaling factor" from Manceau and Nagy (2012) which gives an intensity ratio of 2.39 when S^{6+} and S^{2-} are in exactly equal concentrations. The sulfide and sulfate peaks were each modeled using a single gaussian together with a sigmoid function to account for the edge step. Concentrations were then calculated from the area ratios of the gaussian peaks adjusted by the factor of 2.39 discussed above. Due to the presence of minor amounts of sulfite, a gaussian and sigmoid were also included for S^{4+} and the corrected gaussian area was added to the S^{6+} area. The energy positions and widths of each function were determined from the spectra for the most oxidized and reduced glasses (Fig. 2) which were then fixed for all of the spectral modeling. Uncertainties in $S^{6+}/\Sigma S$ were determined by propagating the standard errors associated with the gaussian peak heights and widths for the fit to each spectrum. A detailed description of the peak fitting method and the modeling results are provided in the Supplementary materials.

The calculated fractions of S^{6+} for each melt at the different fO_2 conditions are shown in Table 2 and plotted against ΔFMQ in Fig. 3. Also shown in Fig. 3 are the theoretical oxygen fugacity

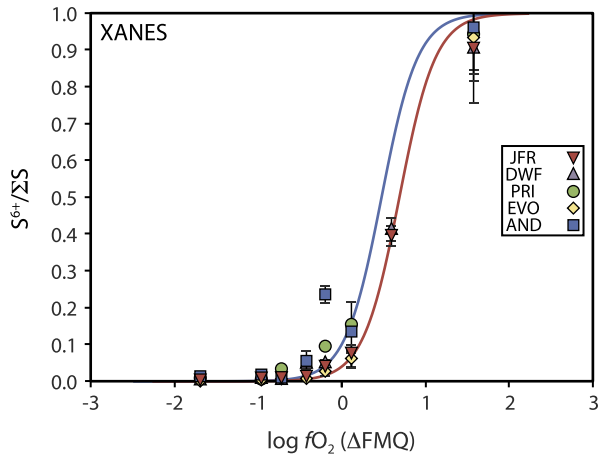

Fig. 3. Fraction of S as S^{6+} determined by XANES spectroscopy plotted against log fO_2 of equilibration relative to the FMQ buffer. Experiments with excessively noisy spectra yielding errors greater than 0.15 $S^{6+}/\Sigma S$ have been omitted from the figure. The smooth curves are best fits to the JFR (red, $R^2 = 0.999$), and AND (blue, $R^2 = 0.958$) assuming a sulfide-oxidation equilibrium of the form given in Equation (8). Errors in sulfate mole fraction have been calculated individually based on the variation in permissible end-member weightings during LCF. Errors in fO_2 are 0.1 log units. (For interpretation of the colors in the figure(s), the reader is referred to the web version of this article.)

curves for addition of $2O_2$ to S^{2-} (as in reaction 7) assuming that activity coefficients for S^{2-} and SO_4^{2-} are constant and unaffected by fO_2. The curves were fitted to the results for the JFR and AND compositions.

Based on the SIMS analyses discussed below we are confident that the conditions of crossover from S^{2-} to S^{6+} are accurately represented by the XANES spectra for 5 of the 6 melts studied. The exception is the dacite melt which appears to contain significant sulfate even at the lowest fO_2 employed (Fig. 2). This result is inconsistent with SIMS results for the dacite (discussed below) which indicate that S^{2-} is dominant at all oxygen fugacities below FMQ+0.13 (Fig. 4). Although we do not have an unequivocal explanation for the aberrant result, we suspect that it arises from a combination of photo-oxidation of the glass during collection of the spectrum and the low concentrations of sulfur in these samples resulting in a low signal to noise ratio. Because of the inconsistency between XANES and SIMS results for dacite we have excluded the S^{6+}/S^{2-} ratios measured by XANES for the DAC glass from data Tables and Fig. 3. The resulting difference in crossover position between melts containing ~5 wt% FeO and those containing ~20 wt% FeO is ~0.5 log units.

4.3. Speciation calculated from sulfur concentration

Total sulfur concentrations measured by SIMS are presented in Table 2, and for the JFR and DAC melts are plotted on a log–log scale against fS_2/fO_2 ratio in Fig. 4. The proportionality relation arising from the sulfide dissolution reaction (Equation (3)) should emerge as a straight line of gradient 1/2 in the data. Points lying above the line reflect increasing S^{6+} in the melt. As observed in earlier studies at 1 atm (Fincham and Richardson, 1954; Katsura and Nagashima, 1974) the S concentration reaches a minimum on approaching the S^{2-} to S^{6+} transition.

As can be seen from Fig. 4, both the DAC and JFR compositions fit the theoretical log [S] versus log (fS_2/fO_2) slope corresponding to dominance of S^{2-} at all fO_2's below FMQ. The same applies for all six melt compositions studied including DAC despite the presence of S^{6+} in the XANES spectrum of this sample, which we attribute to beam damage (Table 2). In order to calculate S^{6+}/S^{2-} for compositions run on Pt loops, we needed to correct for Fe-loss which was significant in some cases (Table 2). To do this we calculated the average sulfide capacity $C_{S^{2-}}$ as defined in Equation (3) for the experiments performed below FMQ. We corrected these $C_{S^{2-}}$ values for observed Fe-loss using the Fe-dependence of sulfur solubility from Smythe et al. (2017) Table 3. We then calculated the expected amounts of S^{2-} at each of the higher fO_2's based on the measured melt compositions at these fO_2's. Additional measured S concentrations above these S^{2-} values were then assumed to be S^{6+} (Table 2). Positive deviations from the predicted "sulfide slope" occur for every melt composition, confirming the presence of an oxidized sulfur species, which our spectroscopic measurements indicate to be S^{6+}. The size of these deviations from the "sulfide slope" and the implied quantities of S^{6+}, are indicated in Fig. 4 by the red arrows. The SIMS data show that the transition from $S^{6+}/\Sigma S$ of <0.05 to $S^{6+}/\Sigma S$ of >0.95 lies between FMQ+0.13 and FMQ+0.62 for all six melts, except for the andesite, which may undergo oxidation at conditions ~0.3 log units more reduced in fO_2. Note, however, that the method is insensitive to small amounts of S^{6+} because of the requirement to fit the 1/2 slope through the data points under the most reducing conditions.

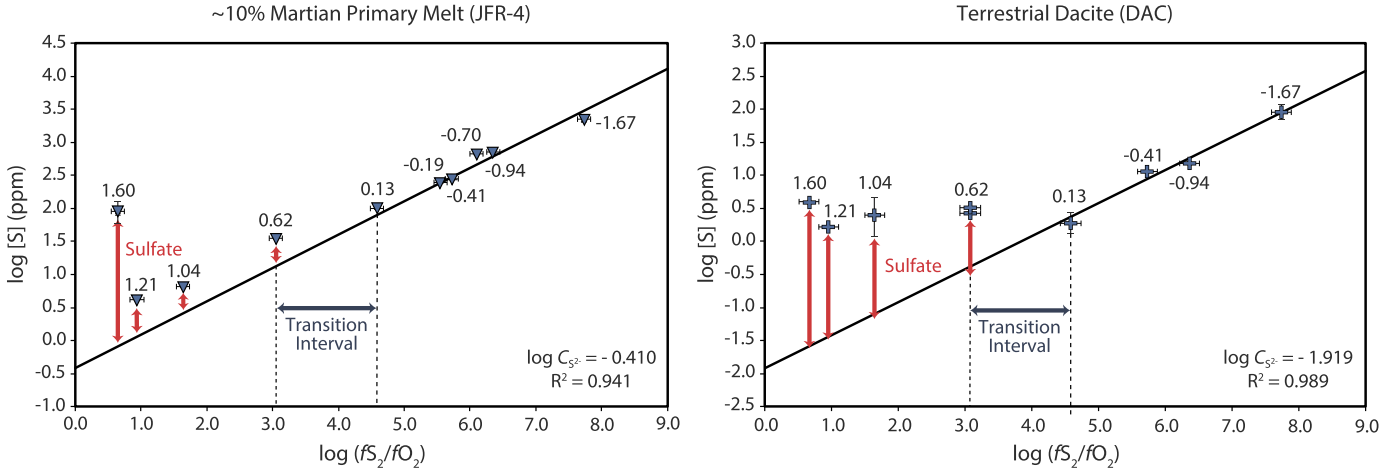

Fig. 4. The logarithm of total sulfur concentration (determined by SIMS) plotted against the logarithm of the fS_2/fO_2 ratio, for the JFR and terrestrial DAC compositions. The fO_2 conditions of each experiment are individually labeled in log units relative to the FMQ buffer. Experiments lying further towards the left represent more oxidizing conditions. The black lines are weighted linear best-fits to experiments equilibrated at FMQ+0.13 and below, with gradients fixed at 1/2, thereby representing the sulfide-dissolution equilibrium (Equations (1)–(3)). Melts with constant sulfide capacity are expected to lie along this slope, and positive deviations are interpreted as indicative of sulfate. Values for log $C_{S^{2-}}$ correspond to the y-intercept (Equation (3)).

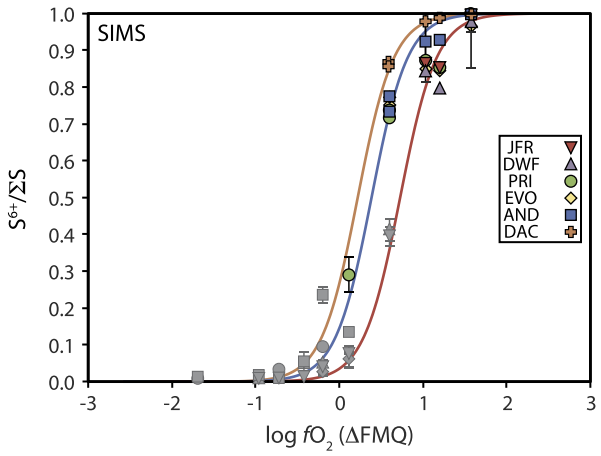

Fig. 5. Fraction of S as S^{6+} derived from SIMS analyses plotted against fO_2. Sulfate mole fractions were determined by subtracting modeled sulfide concentrations from the SIMS analyses of total sulfur (i.e. from the deviations in log [S] from the "sulfide-slopes" in Fig. 4). $S^{6+}/\Sigma S$ of gray symbols were determined by XANES spectroscopy (shown in Fig. 3). The smooth curves are weighted best fits to the JFR (red, $R^2 = 0.997$), AND (blue, $R^2 = 0.980$), and DAC (orange, $R^2 = 0.996$) assuming a sulfide-oxidation equilibrium of the form given in Equation (8). Note that, based on the SIMS results of Fig. 4, the sulfide–sulfate transformation for the DAC composition occurs at similar fO_2 conditions to those of the other 5 melts.

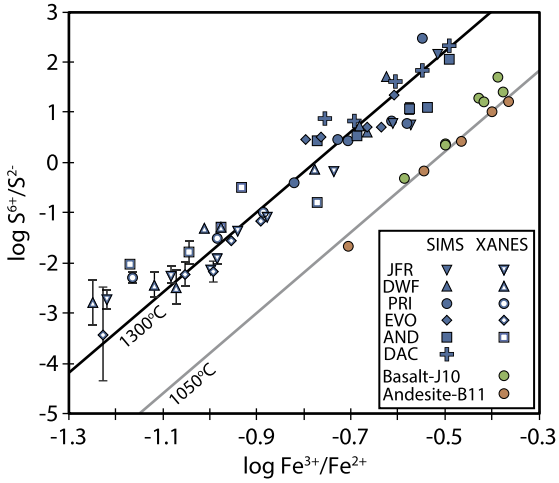

Fig. 6. Variation of log S^{6+}/S^{2-} with log Fe^{3+}/Fe^{2+} for our experimental products. Filled blue symbols represent instances for which S^{6+}/S^{2-} was determined from SIMS data, and unfilled blue symbols represents those for which S^{6+}/S^{2-} was derived from linear combination fitting of XANES spectra. The green and orange symbols represent experiments on basaltic and andesitic melts performed at 1050 °C by Jugo et al. (2010) and Botcharnikov et al. (2011) respectively. All Fe^{3+}/Fe^{2-} ratios are calculated using the formulation of Kress and Carmichael (1991). The black line was fit by weighted linear regression assuming the theoretical electron-exchange relationship of Equation (9) ($R^2 = 0.931$). The gray line was calculated using Equation (11).

This constraint makes the first ~30% of S^{6+} difficult to quantify. The SIMS method is therefore most accurate under oxidizing conditions where the deviations from the 1/2 slope of Fig. 4 are large. This makes the SIMS method complementary to the XANES approach since the latter enables detection of small amounts of S^{6+} but decreases in accuracy at high fO_2 because of the declining sulfur concentrations (Fig. 2).

Fig. 5 shows measurements of sulfur speciation as a function of fO_2 as determined by the sulfur concentration of our samples. We excluded results where the propagated uncertainty exceeded 15% of the $S^{6+}/\Sigma S$ value. As can be seen in Figs. 3 and 5 there is very good agreement between the two methods and a continuous line of crossover from S^{2-} to S^{6+} can readily be constructed. The spread as a function of melt composition is small and behavior of our dacite composition appears to be consistent with that of the other melts.

5. Discussion

5.1. Relationship between of iron and sulfur oxidation states

Fig. 5 shows that $S^{6+}/\Sigma S$ measured in our experiments closely follows the relationship predicted from Equation (8). This is in contrast to measurements performed by electron microprobe (e.g. Carroll and Rutherford, 1988) which are likely affected by the beam-damage discussed earlier (Jugo et al., 2010). Besides sulfur, iron is the only redox-sensitive element present in appreciable concentrations in the glasses investigated. The chemical speciation of these two elements must, therefore, depending on their concentrations, be correlated with one another. The oxidation reactions for sulfur and iron can be combined to yield the following electron-exchange equilibrium:

$$S^{2-} + 8Fe^{3+} = S^{6+} + 8Fe^{2+} \quad (9)$$

as discussed by Métrich et al. (2009) and Jugo et al. (2010). This implies a linear relationship between the logarithms of the activities of S^{6+}/S^{2-} and Fe^{3+}/Fe^{2+} with a gradient of 8, the number of Fe^{3+} ions reduced in oxidizing one S^{2-} to one S^{6+}. Note that Wallace and Carmichael (1992) estimated a much lower slope by using the microprobe S-speciation data of Carroll and Rutherford (1988), but the latter are likely to have been affected by photo-oxidation (Jugo et al., 2010). Sulfur speciation data from both of the methods used in our study, expressed as the logarithm of the concentration ratio S^{6+}/S^{2-} are plotted against calculated values of log (Fe^{3+}/Fe^{2+}) in Fig. 6. The Fe^{3+}/Fe^{2+} ratio for each glass was calculated using the model of Kress and Carmichael (1991), which uses as its input the T, P, fO_2 and major-element composition of the melt.

The experimental results for S^{6+}/S^{2-} shown in Fig. 6 define a line whose gradient approximates that expected from equilibrium (9). The solid line is a best fit with a gradient forced to the theoretical value of 8. The correlation between oxidation states of S and Fe is relatively insensitive to the choice of model for calculating the Fe^{3+}/Fe^{2+} ratio and S^{2-} concentration in each melt; models for Fe^{3+}/Fe^{2+} by Jayasuriya et al. (2004), Sack et al. (1980), and Kress and Carmichael (1991) yield the same trend with similar coefficients of determination, and the effects of using different published coefficients for calculating the compositional dependence of $C_{S^{2-}}$ are similarly minor.

Also shown in Fig. 6 are the data of Jugo et al. (2010) and Botcharnikov et al. (2011) from experiments performed on hydrous basalts and andesites, respectively. These represent equilibrium at a lower temperature (1050 °C) and higher pressure (200 MPa). The S^{6+}/S^{2-} ratios reported by these authors were calculated from XANES spectra, based on a treatment similar to that employed in this study. We estimated Fe^{3+}/Fe^{2+} ratios at the known fO_2's of the experiments by applying the model of Kress and Carmichael (1991), as was done with the glasses from our own experiments. The two studies clearly define linear trends parallel to our data but displaced to lower S^{6+}/S^{2-} by ~2 log units at a given Fe^{3+}/Fe^{2+}.

The differences shown in Fig. 6 between our data, at 1300 °C and 1 atm and those of Jugo et al. (2010) and Botcharnikov et al. (2011) at 1050 °C and 0.2 GPa plausibly arise predominantly from the temperature difference between the studies. This conclusion derives from observations that compositional effects on the S^{6+}/S^{2-}–Fe^{3+}/Fe^{2+} relationship are minor (Fig. 6) and that between 1 bar and 200 MPa pressure effects on redox equilibria are small. The effect of 200 MPa pressure increase on fO_2 difference

between the Ni–NiO (NNO) oxygen buffer and the FMQ buffer at 1300 °C is, for example, only 0.08 log units. In order to elucidate the temperature effect more precisely we formulated Equation (9) in terms of homogeneous equilibrium in the silicate melt using neutral components as follows:

$$FeS + 8FeO_{1.5} = 8FeO + FeSO_4 \quad (10)$$

We then modeled the thermodynamic properties of the melt components using the relevant solids (sulfide, sulfate and oxides) and took data from the JANAF tables (http://kinetics.nist.gov/janaf/) to calculate the temperature effect on reaction (10). We fixed the equilibrium constant at 1300 °C using our experimental data and the best-fit line shown in Fig. 6. The 1050 °C line of Fig. 6 was then calculated (not fitted) based on the displacement down temperature estimated from the thermodynamic data. As can be seen from Fig. 6, the thermodynamic data for the solids enable fair prediction of the temperature effect on equilibrium (10) and we are justified in our assertion that the temperature effect dominates the differences between our results and those of earlier studies. To test the effect of changing sulfide and sulfate components we replaced FeS and $FeSO_4$ in equilibrium (10) by CaS and $CaSO_4$. The calculated temperature effect is in the same direction but slightly smaller, the shift between 1300 °C and 1050 °C being 1.3 instead of 1.8 log units. We get a smaller effect (1.1 log units) if we use FeS, CaO and $FeO_{1.5}$ to produce $CaSO_4$ and FeO. Every equilibrium we have considered gives a substantial temperature effect, however and equilibrium (10) appears to fit the observations well.

The final expression for the relationship between sulfur and iron redox equilibria is:

$$\log\left(\frac{S^{6+}}{S^{2-}}\right) = 8\log\left(\frac{Fe^{3+}}{Fe^{2+}}\right) + \frac{8.7436\times10^6}{T^2} - \frac{27703}{T} + 20.273 \quad (T = 1000 - 2000\ \text{K}) \quad (11)$$

Fig. 7 illustrates the sulfur–iron redox relationship at different temperatures calculated from Equation (11) and expressed as $S^{6+}/\Sigma S$ versus log fO_2 relative to the FMQ buffer. In order to construct Fig. 7 we assumed that Equation (11) is correct and converted Fe^{3+}/Fe^{2+} to fO_2 using the equation of Kress and Carmichael (1991). This approach produces, at any given temperature a range of S^{2-}–S^{6+} transition curves because of the dependence of Fe^{3+}/Fe^{2+} on silicate composition. The effect can be seen clearly in Fig. 7a where the curve for andesite at 1050 °C is separated slightly from that for basalt under the same conditions. Our calculated curves are, nevertheless in remarkably good agreement with the experimental data at 1050 °C. They are also consistent with the results of Matjuschkin et al. (2016) (Fig. 7a) who showed that, in andesitic compositions at 950 °C all S is present as S^{2-} at 0.2–0.4 log units above FMQ and that $CaSO_4$ precipitates at fO_2 above ΔFMQ+~3.4 and +~3.6 at 1.0 and 1.5 GPa, respectively. Using our model this pressure dependence in S^{6+}/S^{2-} is corrected-for by the pressure-dependence of Fe^{3+}/Fe^{2+} given by Kress and Carmichael (1991) and shown as dotted (1.0 GPa) and solid (1.5 GPa) red curves in Fig. 7a. Fig. 7b illustrates the temperature-dependence of crossover behavior at fixed bulk composition and pressure by plotting curves for andesite at temperatures between 900 and 1400 °C. We also show a comparison with our data at 1300 °C.

5.2. The compositional dependence of sulfate capacity

Both the XANES and the SIMS data indicate that the experiments conducted under the most oxidizing conditions (FMQ+1.6) contain sulfur exclusively in the form of sulfate. In aggregate, these experiments therefore demonstrate the dependence of sulfate concentration on melt composition at constant fO_2 and fS_2 (the

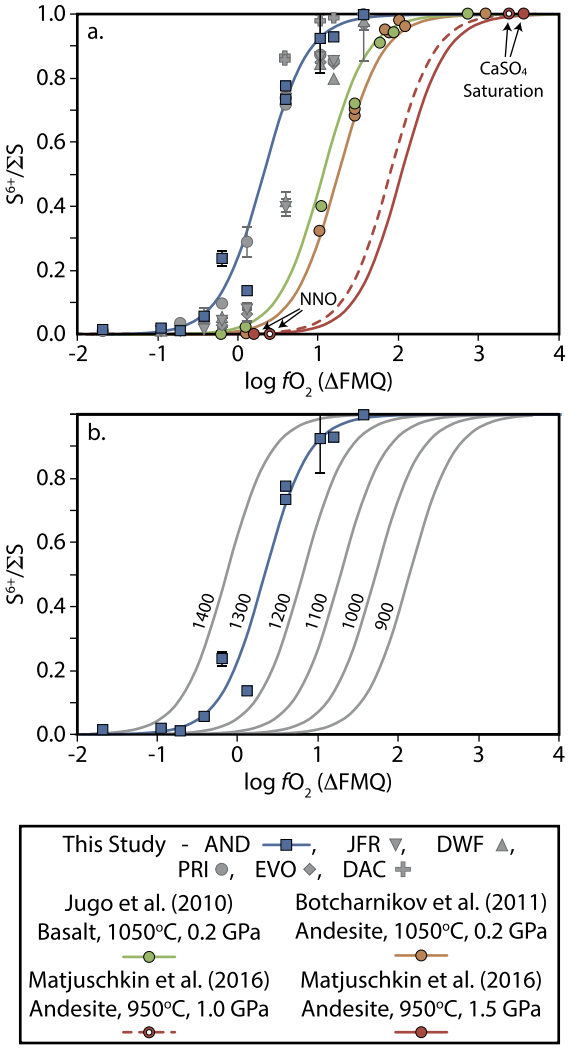

Fig. 7. Summary of sulfide–sulfate transformation intervals as a function of fO_2. Panel (a) provides a compilation of experimental data from this study (blue and gray), Jugo et al. (2010) – green, and Botcharnikov et al. (2011) – orange. The accompanying curves are calculated using the temperature-dependent expression for S^{6+}/S^{2-} as a function of Fe^{3+}/Fe^{2+} (Equation (11)). The red curves are calculated from Equation (11) for the andesitic composition investigated by Matjuschkin et al. (2016) at 950 °C and 1.0 (dashed) and 1.5 GPa. The fO_2 conditions of all S as S^{2-} in the melt and of $CaSO_4$ saturation at 1.0 GPa and 1.5 GPa as determined by Matjuschkin et al. (2016) are shown. Panel (b) shows the expected temperature dependence of Equation (11) with a series of theoretical sulfide–sulfate transformation curves calculated at various temperatures (labeled). The andesite data from the panel above is superimposed, and the appropriate 1300 °C curve highlighted in blue.

'sulfate capacity' of Fincham and Richardson, 1954). A strong negative correlation (R^2 = 0.983) is observed between log [S^{6+}] and the mole fraction of SiO_2 + TiO_2 in the silicate melt calculated on a single cation basis (Fig. 8) at fixed fO_2–fS_2 conditions. The implication is that there are major compositional controls over solubilities of sulfates, with solubility more than 10 times greater in primitive basalt than in evolved dacite. Hence tendency towards saturation in, for example, anhydrite and the degassing of SO_2 are enhanced by fractional crystallization as well as by increased fO_2.

6. Applications

6.1. Oxygen fugacities recorded by quenched melts

The micro-XANES method has been used extensively in recent years to measure the oxidation state of Fe in silicate glasses

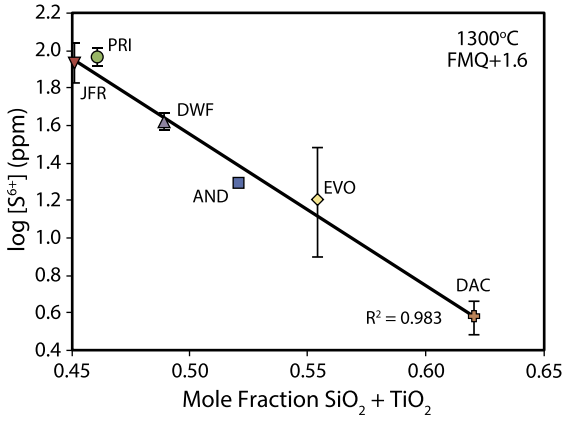

Fig. 8. Covariation between log [S^{6+}] (ppm) and mole fraction of $SiO_2 + TiO_2$ (calculated on a single cation basis) for the six melts equilibrated under the most oxidizing conditions (for which the sulfate species occurs exclusively). As indicated by the black line, the two variables are very strongly correlated ($R^2 = 0.983$). Uncertainties in mole fraction of $SiO_2 + TiO_2$ are smaller than symbols.

and to use these measured Fe^{3+}/Fe^{2+} ratios to estimate the fO_2 of the melt prior to eruption (Cottrell and Kelley, 2011; Kelley and Cottrell, 2009; Plank et al., 2010). We have shown here that there is the expected relationship between the oxidation states of sulfur and iron (Fig. 6) and that this relationship is temperature-dependent. The temperature-dependence translates to the possibility of electron exchange between sulfur and iron during slow cooling of melt. Although sulfur is present at relatively low concentrations (~1500 ppm) in typical basalt, the fact that sulfur has 8 times the redox power of iron per mole (reaction (9)) means that the effects of electron transfer between the two elements can be significant.

For illustration of the effects of electron transfer, we consider glasses from Mauna Kea, Hawaii (Brounce et al., 2017). Brounce et al. (2017) measured the oxidation states of both S and Fe using micro-XANES spectroscopy and demonstrated a decrease in $Fe^{3+}/\Sigma Fe$ from 0.196 to 0.131 with decreasing S content from 1480 to 350 ppm. These changes correspond to decreases in $S^{6+}/\Sigma S$ from 0.08 to 0.00 and an fO_2 decrease from FMQ+1.0 to FMQ-0.45. The authors ascribed the changes in Fe and S oxidation states to reduction caused by degassing, at about 1200 °C, of a C–O–H–S volatile phase which resulted in loss of most of the initial sulfur content. The effects of temperature on the relationships between S^{6+}/S^{2-} and Fe^{3+}/Fe^{2+} ratios which we observe indicate, however, that the effect of S degassing is less dramatic than was estimated by Brounce et al. (2017).

We took the measured S^{6+}/S^{2-} and Fe^{3+}/Fe^{2+} ratios for Mauna Kea glasses from Brounce et al. (2017) and calculated the equilibrium temperature they record as given by Equation (11). For the 31 samples we obtain an average temperature of 993 °C with a standard deviation of 30 °C. Note that if we were to adopt the new Mössbauer calibration of Berry et al. (2018) for Fe^{3+} and Fe^{2+} in basaltic glasses, and re-fit equation (11) using their $Fe^{3+}/\Sigma Fe$ values the apparent equilibrium temperature of the Mauna Kea glasses would increase slightly to 1004 °C. In either case the result indicates that there has been electron exchange between Fe^{2+} and S^{6+} during quenching such that the measured $Fe^{3+}/\Sigma Fe$ and hence estimated fO_2 are now higher than they were at the liquidus temperature. Reconstructing the liquidus $Fe^{3+}/\Sigma Fe$ by assuming, following Brounce et al. (2017), equilibrium between S and Fe at 1200 °C leads to a reduction in $Fe^{3+}/\Sigma Fe$ of the most oxidized S-rich samples by ~0.05, a change much greater than the measurement uncertainty. This shift indicates that the actual fO_2 of the melt was about 0.8 log units lower than implied by the current (quenched) $Fe^{3+}/\Sigma Fe$ values. It implies that the oxidation states of S-rich glasses must be interpreted with care and that S-contents must be measured in tandem with micro-XANES measurements of $Fe^{3+}/\Sigma Fe$.

7. Conclusions

We developed sulfur analysis by SIMS as a method to measure the S^{2-} contents of silicate melts at known fS_2/fO_2. We used this method, together with XANES spectroscopy to determine the effects of fO_2 on the S^{6+}/S^{2-} ratios of six silicate melts, ranging from Fe-rich basalt to dacite in composition at 1300 °C and 1 atm pressure. The two techniques are complementary, in that XANES provides good constraints on S^{6+} contents at low S^{6+}/S^{2-} while the SIMS method provides better results at high S^{6+}/S^{2-} ratio.

We find that the S^{6+}/S^{2-} ratio in silicate melts is, at fixed fO_2, almost independent of melt composition. Despite the well-established correlation between S-solubility and FeO concentration (O'Neill and Mavrogenes, 2002) we have found that in basaltic melts containing up to 20 wt% FeO, the transition from S^{2-} to S^{6+} takes place at an fO_2 only ~0.5 log units higher than in dacitic melts containing 5 wt% FeO. Thus, the stabilizing effect of FeO on S^{2-} in silicate melt is not reflected in S^{6+}/S^{2-} at given fO_2. The principal reason likely derives from our observation that SO_4^{2-} concentration is, at fixed, fO_2, fS_2 conditions negatively correlated with tetrahedral ($SiO_2 + TiO_2$) concentration (Fig. 8). Thus, S^{2-} stabilization in natural FeO-rich melts is counterbalanced by stabilization of SO_4^{2-} in these correspondingly low-SiO_2 melts. Conversely, destabilization of S^{2-} in FeO-poor dacitic melts is counterbalanced by destabilization of SO_4^{2-} in these high SiO_2 liquids.

Although melt composition has little effect on the fO_2 at which S^{2-} is oxidized to SO_4^{2-}, the effect of temperature is dramatic. Thus, a decrease in temperature from 1300 to 1100 °C displaces the S^{2-} to S^{6+} transition upwards by about 1 log unit in fO_2 relative to the FMQ buffer. S^{6+}/S^{2-} ratios for the quenched melts also exhibit a linear relationship with Fe^{3+}/Fe^{2+}, indicating that the redox couples for iron and sulfur can be directly related to one another.

The interdependence of the oxidation states of S and Fe means that the application of measurements of Fe^{3+}/Fe^{2+} in quenched glasses to estimate the fO_2 of natural melts may lead to significant errors. Based on XANES measurements of Fe^{3+}/Fe^{2+} and S^{6+}/S^{2-} in glasses from Mauna Kea, Hawaii we find that there was significant exchange of electrons between S and Fe during quenching. The effect is sufficient to cause significant overestimation of equilibrium $Fe^{3+}/\Sigma Fe$ in the glasses and corresponding overestimate of fO_2 by ~0.8 log units.

Acknowledgements

We acknowledge the award to WN of a studentship by the Science and Technology Facilities Council (UK). DS and BJW were funded by Natural Environment Research Council grants NE/M000427/1 and NE/P017371/1 (FAMOS). We thank P. Jugo and H. O'Neill for their thorough reviews.

Appendix A. Supplementary material

Supplementary material related to this article can be found online at https://doi.org/10.1016/j.epsl.2018.12.006.

References

Almkvist, G., Boye, K., Persson, I., 2010. K-edge XANES analysis of sulfur compounds: an investigation of the relative intensities using internal calibration. J. Synchrotron Radiat. 17, 683–688.

Bertka, C.M., Holloway, J.R., 1994. Anhydrous partial melting of an iron-rich mantle II: primary melt compositions at 15 kbar. Contrib. Mineral. Petrol. 115, 323–338.
Berry, A.J., Stewart, G.A., O'Neill, H.St.C., Mallmann, G., Mosselmans, J.F.W., 2018. A re-assessment of the oxidation state of iron in MORB glasses. Earth Planet. Sci. Lett. 383, 114–123.
Botcharnikov, R.E., Linnen, R.L., Wilke, M., Holtz, F., Jugo, P.J., Berndt, J., 2011. High gold concentrations in sulphide-bearing magma under oxidizing conditions. Nat. Geosci. 4, 112–115.
Brounce, M., Stolper, E., Eiler, J., 2017. Redox variations in Mauna Kea lavas, the oxygen fugacity of the Hawaiian plume, and the role of volcanic gases in Earth's oxygenation. Proc. Natl. Acad. Sci. USA 114, 8997–9002.
Carmichael, I.S.E., Turner, F.J., Verhoogen, J., 1974. Igneous Petrology. McGraw-Hill.
Carmichael, I.S.E., 1991. The redox states of basic and silicic magmas – a reflection of their source regions. Contrib. Mineral. Petrol. 106, 129–141.
Carroll, M.R., Rutherford, M.J., 1988. Sulfur speciation in hydrous experimental glasses of varying oxydation states: results from measured wavelength shifts of sulfur X-rays. Am. Mineral. 73, 845–849.
Chase Jr., M.W., Davies, C.A., Downey Jr., J.R., Frurip, D.J., McDonald, R.A., Syverud, A.N., 1985. JANAF thermochemical tables third edition. J. Phys. Chem. Ref. Data 14 (Supplement 1). 1856 pp.
Cottrell, E., Kelley, K.A., 2011. The oxidation state of Fe in MORB glasses and the oxygen fugacity of the upper mantle. Earth Planet. Sci. Lett. 305, 270–282.
Dreibus, G., Palme, H., 1995. Cosmochemical constraints on the sulfur contents of the Earth's core. Geochim. Cosmochim. Acta 60, 125–130.
Dreibus, G., Wanke, H., 1985. Mars, a volatile-rich planet. Meteoritics 20, 367–381.
Fincham, C.J.B., Richardson, F.D., 1954. The behaviour of sulphur in silicate and aluminate melts. Proc. R. Soc. A, Math. Phys. Eng. Sci. 223, 40–62.
Fleet, M.E., Liu, X., Harmer, S.L., King, P.L., 2005. Sulfur K-edge XANES spectroscopy: chemical state and content of sulfur in silicate glasses. Can. Mineral. 43, 1605–1618.
Gale, A., Dalton, C.A., Langmuir, C.H., Su, Y., Schilling, J-G., 2013. The mean composition of ocean ridge basalts. Geochem. Geophys. Geosyst. 14, 489–518.
Jalilehvand, F., 2006. Sulfur: not a "silent" element any more. Chem. Soc. Rev. 35, 1256–1268.
Jayasuriya, K.D., O'Neill, H.St.C., Berry, A.J., Campbell, S.J., 2004. A Mössbauer study of the oxidation state of Fe in silicate melts. Am. Mineral. 89, 1597–1609.
Jugo, P.J., Wilke, M., Botcharnikov, R.E., 2010. Sulfur K-edge XANES analysis of natural and synthetic basaltic glasses: implications for S speciation and S content as function of oxygen fugacity. Geochim. Cosmochim. Acta 74, 5926–5938.
Katsura, T., Nagashima, S., 1974. Solubility of sulfur in some magmas at 1 atmosphere. Geochim. Cosmochim. Acta 38, 517–531.
Kelley, K.A., Cottrell, E., 2009. Water and the oxidation state of subduction zone magmas. Science 325, 605–607.
Kiseeva, E.S., Wood, B.J., 2013. A simple model for chalcophile element partitioning between sulphide and silicate liquids with geochemical applications. Earth Planet. Sci. Lett. 383, 68–81.
Kiseeva, E.S., Wood, B.J., 2015. The effects of composition and temperature on chalcophile and lithophile element partitioning into magmatic sulphides. Earth Planet. Sci. Lett. 424, 280–294.
Klimm, K., Kohn, S.C., O'Dell, L.A., Botcharnikov, R.E., Smith, M.E., 2012a. The dissolution mechanism of sulphur in hydrous silicate melts. I: assessment of analytical techniques in determining the sulphur speciation in iron-free to iron-poor glasses. Chem. Geol. 322–323, 237–249.
Klimm, K., Kohn, S.C., O'Dell, L.A., Botcharnikov, R.E., Smith, M.E., 2012b. The dissolution mechanism of sulphur in hydrous silicate melts. II: solubility and speciation of sulphur in hydrous silicate melts as a function of fO_2. Chem. Geol. 322–323, 250–267.
Kress, V.C., Carmichael, I.S.E., 1991. The compressibility of silicate liquids containing Fe_2O_3 and the effect of compositions, temperature, oxygen fugacity and pressure on their redox states. Contrib. Mineral. Petrol. 108, 82–92.
Li, C., Ripley, E.M., 2005. Empirical equations to predict the sulfur content of mafic magmas at sulfide saturation and applications to magmatic sulfide deposits. Miner. Depos. 40, 218–230.
Manceau, A., Nagy, K.L., 2012. Quantitative analysis of sulfur functional groups in natural organic matter by XANES spectroscopy. Geochim. Cosmochim. Acta 99, 206–223.
Mathez, E.A., 1976. Sulfur solubility and magmatic sulfides in submarine basalt glass. J. Geophys. Res. 81, 4269–4276.
Matjuschkin, V., Blundy, J.D., Brooker, R.A., 2016. The effect of pressure on sulfur speciation in mid- to deep-crustal arc magmas and implications for the formation of porphyry copper deposits. Contrib. Mineral. Petrol. 171, 1–25.
McSween, H.Y., Wyatt, M.B., Gellert, R., Bell III, J.F., Morris, V.R., Herkenhoff, K.E., Crumpler, L.S., Milam, K.A., Stockstill, K.R., Tornabene, L.L., Arvidson, R.E., Bartlett, P., Blaney, D., Cabrol, N.A., Christensen, P.R., Clark, B.C., Crisp, J.A., Des Marais, D.J., Economou, T., Farmer, J.D., Farrand, W., Ghosh, A., Golombek, M., Gorevan, S., Greeley, R., Hamilton, V.E., Johnson, J.R., Joliff, B.L., Klingelhöfer, G., Knudson, A.T., McLennan, S., Ming, J.E., Moersch, J.E., Rieder, R., Ruff, S.W., Schröder, C., de Souza Jr., P.A., Squyres, S.W., Wänke, H., Wang, A., Yen, A., Zipfel, J., 2006. Characterization and petrologic interpretation of olivine-rich basalts at Gusev Crater, Mars. J. Geophys. Res. 111, E02S10.
Métrich, N., Bonnin-Mosbah, M., Susini, J., Menez, B., Galoisy, L., 2002. Presence of sulfite (S^{IV}) in arc magmas: implications for volcanic sulfur emissions. Geophys. Res. Lett. 29.
Métrich, N., Berry, A.J., O'Neill, H.St.C., Susini, J., 2009. The oxidation state of sulfur in synthetic and natural glasses determined by X-ray absorption spectroscopy. Geochim. Cosmochim. Acta 73, 2382–2399.
Nittler, L.R., Starr, R.D., Weider, S.Z., McCoy, T.J., Boynton, W.V., Ebel, D.S., Ernst, C.M., Evans, L.G., Goldsten, J.O., Hamara, D.K., Lawrence, D.J., McNutt Jr., R.L., Schlemm II, C.E., Solomon, S.C., Sprague, A.L., 2011. The major-element composition of Mercury's surface from MESSENGER X-ray spectrometry. Science 333, 1847–1850.
O'Neill, H.St.C., 1987. Quartz–fayalite–iron and quartz–fayalite–magnetite equilibria and the free energy of formation of fayalite (Fe_2SiO_4) and magnetite (Fe_3O_4). Am. Mineral. 72, 67–75.
O'Neill, H.St.C., Mavrogenes, J.A., 2002. The sulfide capacity and the sulfur content at sulfide saturation of silicate melts at 1400 °C and 1 bar. J. Petrol. 43, 1049–1087.
Palme, H., O'Neill, H.St.C., 2014. Cosmochemical estimates of mantle composition. In: Treatise on Geochemistry, 2nd ed., pp. 1–39. Ch. 3.1.
Paris, E., Giuli, G., Carroll, M.R., 2001. The valence and speciation of sulfur in glasses by X-ray absorption spectroscopy. Can. Mineral. 39, 331–339.
Plank, T., Zimmer, M., Cottrell, E., Kelley, K., 2010. The oxidation state of magmas from melt inclusions and olivine hosts. Geochim. Cosmochim. Acta 74, A819.
Sack, R.O., Carmichael, I.S.E., Rivers, M., Ghiorso, M.S., 1980. Ferric-ferrous equilibria in natural silicate liquids at 1 bar. Contrib. Mineral. Petrol. 75, 369–376.
Smythe, D.J., Wood, B.J., Kiseeva, E., 2017. The S content of silicate melts at sulfide saturation: new experiments and a model incorporating the effects of sulfide composition. Am. Mineral. 102, 795–803.
Wallace, P.J., Carmichael, I.S.E., 1992. Sulfur in basaltic magmas. Geochim. Cosmochim. Acta 56, 1863–1874.
Wendlant, R.F., 1982. Sulfide saturation of basalt and andesite melts at high pressures and temperatures. Am. Mineral. 67, 877–885.
Wilke, M., Jugo, P.J., Klimm, K., Susini, J., Botcharnikov, R., Kohn, S.C., Janousch, M., 2008. The origin of S^{4+} detected in silicate glasses by XANES. Am. Mineral. 93, 235–240.
Wilke, M., Klimm, K., Kohn, S.C., 2011. Spectroscopic studies on sulfur speciation in synthetic and natural glasses. Rev. Mineral. Geochem. 73, 41–78.
White, W.B., Johnson, S.M., Dantzig, G.B., 1958. Chemical equilibrium in complex mixtures. J. Chem. Phys. 28, 751–755.
Wohlers, A., Wood, B.J., 2017. Uranium, thorium and REE partitioning into sulfide liquids: implications for reduced S-rich bodies. Geochim. Cosmochim. Acta 205, 226–244.
Wojdyr, M., 2010. Fityk: a general-purpose peak fitting program. J. Appl. Crystallogr. 43, 1126–1128.